Available online at www.sciencedirect.com
SCIENCE DIRECT®
ELSEVIER
Ultramicroscopy 104 (2005) 73–82
ultramicroscopy
www.elsevier.com/locate/ultramic

On the peculiarities of CBED pattern formation revealed by multislice simulation

A. Chuvilin*, U. Kaiser

University of Ulm, Albert-Einstein-Alee 11, D-89081 Ulm, Germany

Received 9 September 2004; received in revised form 18 February 2005; accepted 2 March 2005

Abstract

A modified multislice method has been developed for calculations of Convergent Beam Electron Diffraction (CBED) patterns. The validity of the method for HOLZ- and Kikuchi-line calculations has been proofed by comparison to Bloch-wave calculations. The application of the method leads to the new understanding of CBED patterns formation. Dynamical scattering of weak HOLZ reflections plays the key role in the appearance of deficient lines in the central CBED disk. Different HOLZ lines do have significantly different and extended scattering areas; the central 000 CBED disk, consequently, contains structural information from an area around the primary beam which is determined by the Bragg angle of HOLZ reflections and the thickness of the sample. A variation of lattice parameters, if present within this area, results in artificial symmetry violations of the pattern and in changes of line profiles.

PACS: 61.14.Lj; 61.14.Dc

Keywords: CBED; Strain; HOLZ lines; Multislice

1. Introduction

Convergent Beam Electron Diffraction (CBED) is a TEM technique with a wide range of unique capabilities. It can be applied for crystal symmetry determination [1], polarity determination of non-centrosymmetric crystals [2], temperature factors [3,4] and charge density refinement [5,6], dislocations and interface study [7–9], lattice parameter determination [10,11] and local strain analysis [12,13]. A few tasks, such as symmetry group or polarity determination, can be solved by direct interpretation of CBED patterns. However, for most of the tasks, especially if quantitative results are required, dynamical calculations of CBED patterns have to be performed, which are mainly based on the Bloch-wave approach [14,15] so far.

*Corresponding author. Tel.: +49 731 50 22941; fax: +49 731 50 22958.
E-mail address: andrey.chuvilin@physik.uni-ulm.de (A. Chuvilin).

0304-3991/$ - see front matter © 2005 Elsevier B.V. All rights reserved.
doi:10.1016/j.ultramic.2005.03.003

Progress in semiconductor micro- and nanotechnology requires tools for the reliable local measurement of mechanical strains in semiconductor devices. The increasing popularity of the CBED method for this purpose is addressed to the thought that CBED patterns contain structural information from a column along the beam direction with a diameter of the area illuminated by the primary and strong diffracted beams [16]. Advances in field emission electron sources and electron optics made subnanometer size probes practically available, and thus strain fields in semiconductor devices might be measured with the spatial resolution of 1 nm. However, a number of phenomena have been observed in CBED patterns of imperfect crystals, which cannot be understood in the frame of this idea, as e.g. line splitting [17,18], unexpected symmetry violations [12] and HOLZ line blurring near the interfaces [19]. The Bloch wave theory cannot describe the scattering by imperfect crystals without further approximations, because of a huge number of Bloch states in this case and thus enormous computational expenses.

The multislice method was suggested as an alternative for calculating nanodiffraction [20]. Advantage of the multislice method is that it does not require particular approximations for imperfect crystals and thus electron scattering for the distorted crystals can be calculated to the same accuracy as for the perfect ones. Muller et al. [21] applied the multislice method to calculate correlated-phonon background in CBED patterns. Thus it was shown, that real-space information (correlation of displacements of atoms from outlying unit cells) is presented in experimental CBED patterns and can be reproduced using the multislice method. Also using the multislice method, Spence et al. [22,23] simulated successfully superstructural Laue rings from dislocation cores.

Here we demonstrate, that the multislice method can simulate correctly deficient HOLZ lines in the central CBED disk as well. Consequences of this approach seem to be of general value for the understanding of the process of CBED pattern formation and in particular to answer the question of how local a CBED pattern can be.

2. Methods

All simulations were performed with the homemade program "Mulsi" based on the implementation of FFT multislice algorithm. The algorithm was modified in accordance to Refs. [21,24] in order to optimise the speed of CBED calculations. "Mulsi" runs under Win2Kpro and higher on common use PCs. Depending on the hardware, the program allows at reasonable time (from a few hours to a few days on a P4 2.8 HT/2G RAM PC) the calculation of HR images and CBED patterns up to $8K \times 8K$ pixels in size of models consisting of up to 10^8 independent atoms.

The idea to calculate the propagation of a sharp electron probe with the multislice method was first introduced by Spence [20] and was utilized later for CBED [25] as well as for ADF STEM image calculations [26]. A focused probe is represented by a disk in reciprocal space (corresponding to electron wave filling the condenser aperture), rather than a delta function (plane wave) used for CTEM image simulations. The diameter of the disk determines the convergence angle of illuminating beam and the disk position determines the beam tilt. The modulation of the phase of the complex wave function within the disk allows accounting for lens aberrations and probe position in real space. The probe wave function in the real space is then obtained by a backward Fourier transformation.

Particular requirements for the calculation parameters have to be fulfilled in order to calculate CBED patterns including HOLZ lines. The sampling frequency in real space is determined by the scattering angle of the highest order lines included in the simulation. In order to account for the reflection with a particular g-vector of $G\,nm^{-1}$, the sampling interval of the phase grating should be smaller than $1/(2\,G)$ nm. For typical g-vectors of HOLZ lines of about $50\,nm^{-1}$, a sampling of at least 0.01 nm is required (which is similar to the requirements for HRTEM image calculations). The sampling interval in reciprocal space is determined by a desired resolution of HOLZ lines. In order to image a first-order Laue zone line (which is typically about $0.05\,nm^{-1}$ wide) with a width of at least two pixels, the sampling interval

should be $0.025\,nm^{-1}$. The latter determines the minimum supercell size in real space to be of the order of 40 nm. Larger supercells are required for the higher order lines imaging. This requirement can be reformulated as follows: the supercell should be large enough in order to include all the HOLZ lines intensities scattered at a destination thickness. Thus, the calculation of a HOLZ line scattering to $50\,nm^{-1}$ (about 10° at 100 kV) for a thickness of 150 nm with a probe positioned at the center of the supercell will require a size of the supercell of $2*150*\tan(10^\circ) \sim 53$ nm.

Slicing schemes used for HRTEM image simulations were incapable to calculate HOLZ lines correctly [27,28] so far. This is mainly due to the fact that equal slice thicknesses used in traditional multislice algorithm in most cases require a "shift" of atomic potential in Z direction (see Fig. 1). Thus, the 3D symmetry of the crystal under investigation appears to be broken. As far as HOLZ lines reflect not a projection symmetry, but the full 3D symmetry of the crystal [1], "equal thickness" scheme cannot simulate HOLZ lines correctly by definition. We implemented a scheme, which calculates the projection of the atomic potential "in-place", i.e. potentials of atoms from each atomic layer are projected into the separate phase grating, with its z-coordinate equal to the z-coordinate of the layer. In this case, z-coordinates of atoms in real space and hence 3D symmetry of a crystal, positions and intensities of HOLZ lines in reciprocal space are preserved. The propagation between phase gratings is then calculated in a common way.

Test calculations were performed for Si [1 1 1] at a specimen thickness of 150 nm at 100 kV. The Doyle–Turner formula [29] was used for the potential calculation, the Debye–Waller factor equal to $0.003\,nm^2$ was used to account for thermovibrations and the absorption was set to zero. A supercell with a size of $40 \times 40\,nm^2$ was calculated on a matrix of $4K \times 4K$. The probe diameter at the entrance plane was about 0.3 nm. Fig. 2 demonstrates the comparison of a multislice simulation and a Bloch-wave simulation performed with the "mbfit" program [14] for the same set of parameters. HOLZ lines positions and intensities calculated by multislice correspond well to those calculated by the Bloch-waves method. The thickness fringes differ by a thickness of about 2 nm, which is probably due to a parabolic propagator approximation used in multislice. Such a good agreement between two simulations is remarkable, as each pattern is created in a very

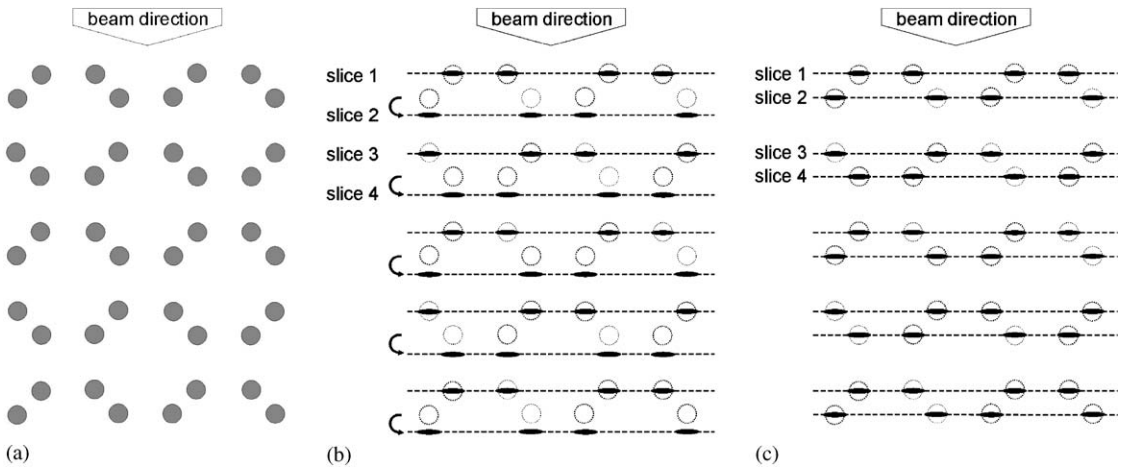

Fig. 1. Illustration of slicing scheme used in multislice simulations: (a) example structure, (b) traditional slicing scheme with equal slice thickness; projected potentials are shifted in Z direction (indicated by the arrows) relative to atoms in the model; only 2D symmetry of projection is preserved and (c) suggested slicing scheme with varying slice thickness; Z-positions of atoms are preserved and thus full 3D symmetry of the crystal is preserved.

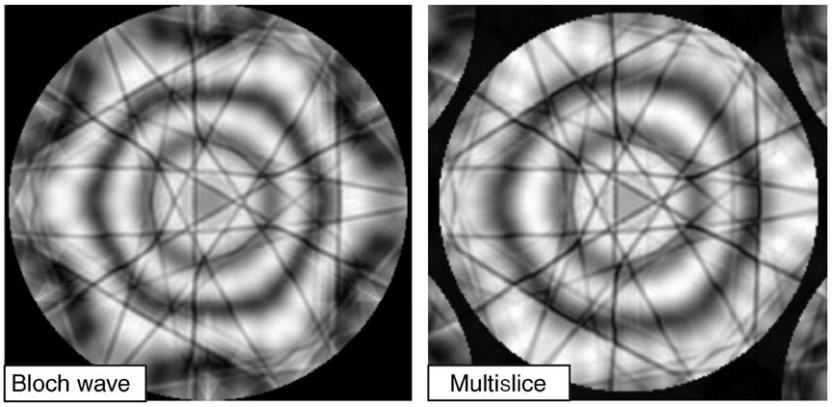

Fig. 2. Comparison of Bloch-wave and multislice simulation methods. [1 1 1] CBED pattern of Si is simulated for 100 kV. Crystal thickness is 150 nm, Doyle–Turner scattering factors are used, Debye–Waller factor is set to 0.003 nm^2, no absorption. For multislice simulation, the size of the supercell is $40 \times 40\,nm^2$, the matrix size is $4K \times 4K$ pixels, the convergence semi-angle is $2.5\,nm^{-1}$, no lens aberrations are applied.

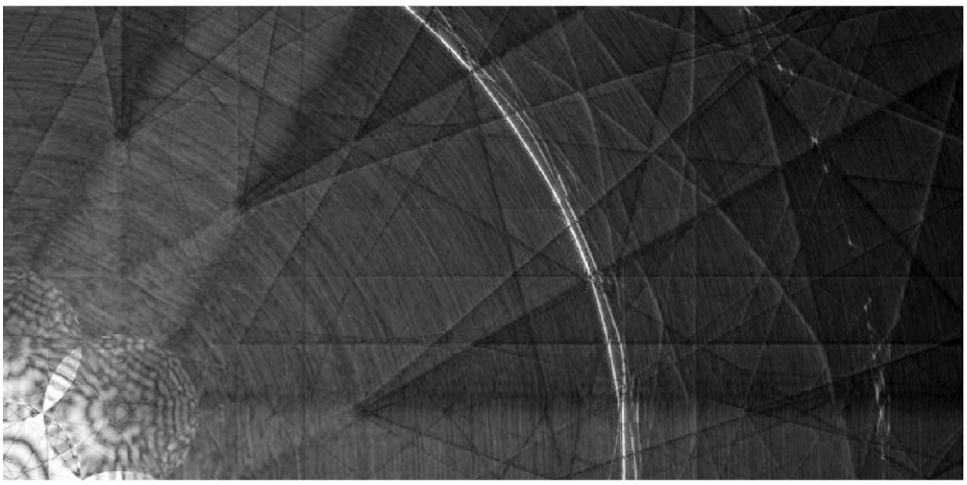

Fig. 3. Multislice simulation similar to Fig. 2, but instead of the Debye–Waller factor, the frozen phonon (uncorrelated) model is used to account for thermovibrations. Convergence semi-angle is $3\,nm^{-1}$ herein. Thirty different phonon configurations are averaged to obtain the pattern. Image intensity is gamma corrected in order to represent both lights and shadows.

different way: Bloch-waves method calculates CBED pattern point by point (using independent plane wave approximation), stacking results of independent calculations in a CBED disk, whereas multislice produces the pattern as a whole by Fourier transformation of a coherent exit wave.

Diffraction phenomenon, which is closely related to HOLZ lines, is a Kikuchi pattern. It has been demonstrated earlier that the multislice method can correctly calculate Kikuchi bands, if the frozen phonons model [30] is used, and even the detailed structure of the bands can be reproduced by applying a ''true'' correlated phonon spectrum [21]. Using the frozen phonon model and the slicing scheme suggested here, it is possible to calculate the full picture of elastic diffuse background including fine Kikuchi lines (see Fig. 3). However, further on in the paper we will use only the Debye–Waller-factor approximation in order to minimize calculation time.

3. Results and discussion

As the multislice algorithm operates in real and reciprocal space, it allows establishing a direct relation between the scattered beams (reciprocal space) and the region of scattering (real space). Fig. 4 illustrates the propagation of a 0.3 nm probe through Si in [1 1 1] direction. While the main intensity is preserved within 1–2 nm around the central beam (at 150 nm depth), weak beams scatter as far as 15 nm away from the center. Fig. 5a represents the reciprocal space picture, i.e. the CBED pattern, corresponding to the wave at Fig. 4c. The excessive $\langle \bar{1}\,1\,5\,5 \rangle$ FOLZ line (marked by rectangular at Fig. 5a) is represented by a cross-section of the well-developed dispersion surface (Fig. 5b), which clearly indicates the dynamical nature of the scattering. A dark field image (Fig. 5c), numerically reconstructed for this $\langle \bar{1}\,1\,5\,5 \rangle$ line, shows that the scattering of this line occurs within a narrow region stretched 15 nm away from the center to the direction of the g-vector of the corresponding reflection. Other lines similarly have their distinct scattering regions. The size of these regions is determined by t*tan(2Θ), where t is the sample thickness and Θ is a Bragg angle for the particular line.

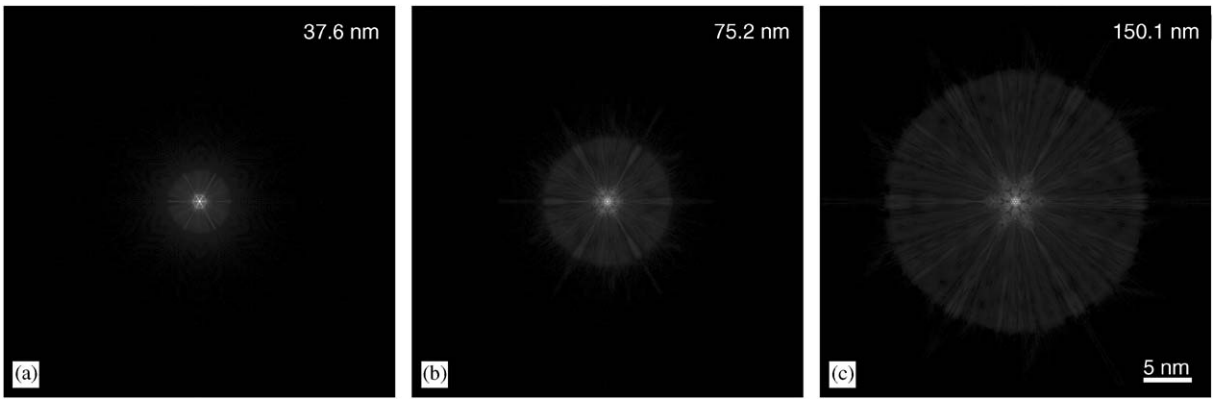

Fig. 4. Propagation of 0.3 nm electron probe along the [1 1 1]-zone axis of Si. Simulation parameters are identical to Fig. 2, besides the 3 nm^{-1} beam convergence semi-angle. Intensity is represented in logarithmic scale. Values at the top-right indicate the crystal thickness.

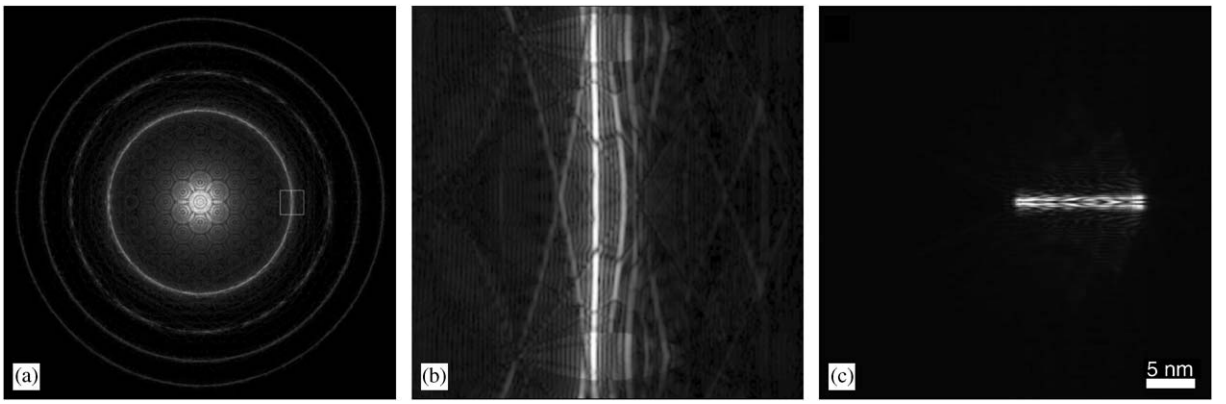

Fig. 5. (a) [1 1 1] Si CBED pattern corresponding to the exit wave at 150 nm at Fig. 4, (b) $\langle \bar{1}\,1\,5\,5 \rangle$ type excess line (marked with rectangular at (a)) demonstrating well-developed dispersion surface and (c) dark-field image reconstructed for the $\langle \bar{1}\,1\,5\,5 \rangle$ line, showing the area from which the line is scattered from (compare to Fig. 4c).

So far, however, it is not worked-out whether back scattering from weak HOLZ beams into the central beam occurs and to what extent this backscattering may influence the intensity distribution in the central disk. In other words, whether the central disk contains structural information only from the volume, which is illuminated by the primary beam, or in addition from the neighboring regions?

To clarify this point, we cut off the part of the crystal model, where the scattered $\langle \bar{1}\,1\,5\,5 \rangle$ reflection was propagating, thus directly preventing secondary scattering for this reflection (see Fig. 6). The cut was made 3 nm away from the illumination cone, so that zero-order reflections with small scattering angles are not influenced. The wave obtained at the exit plane of 150 nm thick crystal (Fig. 7a) looks similar to the case of the bulk crystal (Fig. 4c), as does the CBED pattern (Fig. 7b). However, there is a difference revealed by subtraction of the two waves as seen in Fig. 7c. There is also a difference in the shape of the excessive HOLZ lines (see Fig. 7d for $\langle \bar{1}\,1\,5\,5 \rangle$), which diffracted to the direction of the edge, i.e. went out off the crystal shortly after primary scattering. This line is no more a slice of the dispersion surface (compare to Fig. 5b), but is an arc of a circle, which can be thought of as an intersection of the Ewald sphere with the first Laue zone. This indicates clearly the kinematical behavior of scattering in this case. At the same time the deficient HOLZ lines in the central CBED disk, with the g-vectors pointing to the edge, change dramatically due to the proximity of the edge, the others stay unaffected (Fig. 8). These lines marked by the arrows in Fig. 8a, blur and completely vanish at Fig. 8b. This phenomenon was observed experimentally in CBED patterns taken close to incoherent interface boundaries [19]. Thus, we may conclude that deficient HOLZ lines in the central CBED disk arise only due to the secondary scattering of HOLZ reflections, a kinematical scattering of the primary beam itself does not result in sharp deficient lines as it was thought so far. The other conclusion is that deficient lines are formed outside the cone of primary illuminating beam and therefore should reflect lattice parameters not at the beam position, but in adjacent regions.

As different HOLZ lines originate from different azimuth directions, the position of each line reflects the lattice parameters in its particular scattering region. Hence, the central CBED disk **combines,** but not averages, structural information from some area around the beam. This means, that relative line positions reflect not only the lattice parameters, but also the gradient of lattice parameters. In addition, the variation of lattice parameters within the scattering area should influence the intensity profile of the lines as well.

To illustrate the practical consequences of such scattering delocalization for the case of CBED, we simulated the diffraction pattern of a crystal with a strain gradient. The atomic model was made for a Si crystal strained in [1 1 0] direction with the strain gradient of $4.3 \times 10^{-4}\,\mathrm{nm}^{-1}$. Thus, for a supercell of a length of 47 nm in [1 1 0] direction, the crystal had a tensile strain of 10^{-2} at the left side of the supercell, was unstrained in the middle (at the position of the illuminating beam) and had a compressive strain of 10^{-2} at the right side of the cell. The CBED pattern was simulated for Si [3 3 1] at 100 kV, a supercell of $47 \times 47\,\mathrm{nm}^2$ was sampled into a $4\mathrm{K} \times 4\mathrm{K}$ matrix, the semi-angle of convergence was 15 mrad, the crystal thickness was 237 nm and accelerating voltage was 100 kV. For comparison, the [3 3 1] CBED pattern for the perfect unstrained crystal was calculated using the same simulation parameters. Fig. 9 compares these two simulated CBED patterns. The strain gradient leads to HOLZ lines splitting as well as to symmetry violation. FOLZ lines, however, are mostly unaffected at this zone due to their low scattering angles. Such kind of splitting was often observed in experimental CBED patterns in combination with the symmetry violation [12,31]. In most cases, splitting was ignored until it grew to extreme values and symmetry violations were explained in terms of shear strain components. However, in accordance to the calculation presented, it is more likely that the observation of these two effects together indicates the presence of a strain gradient.

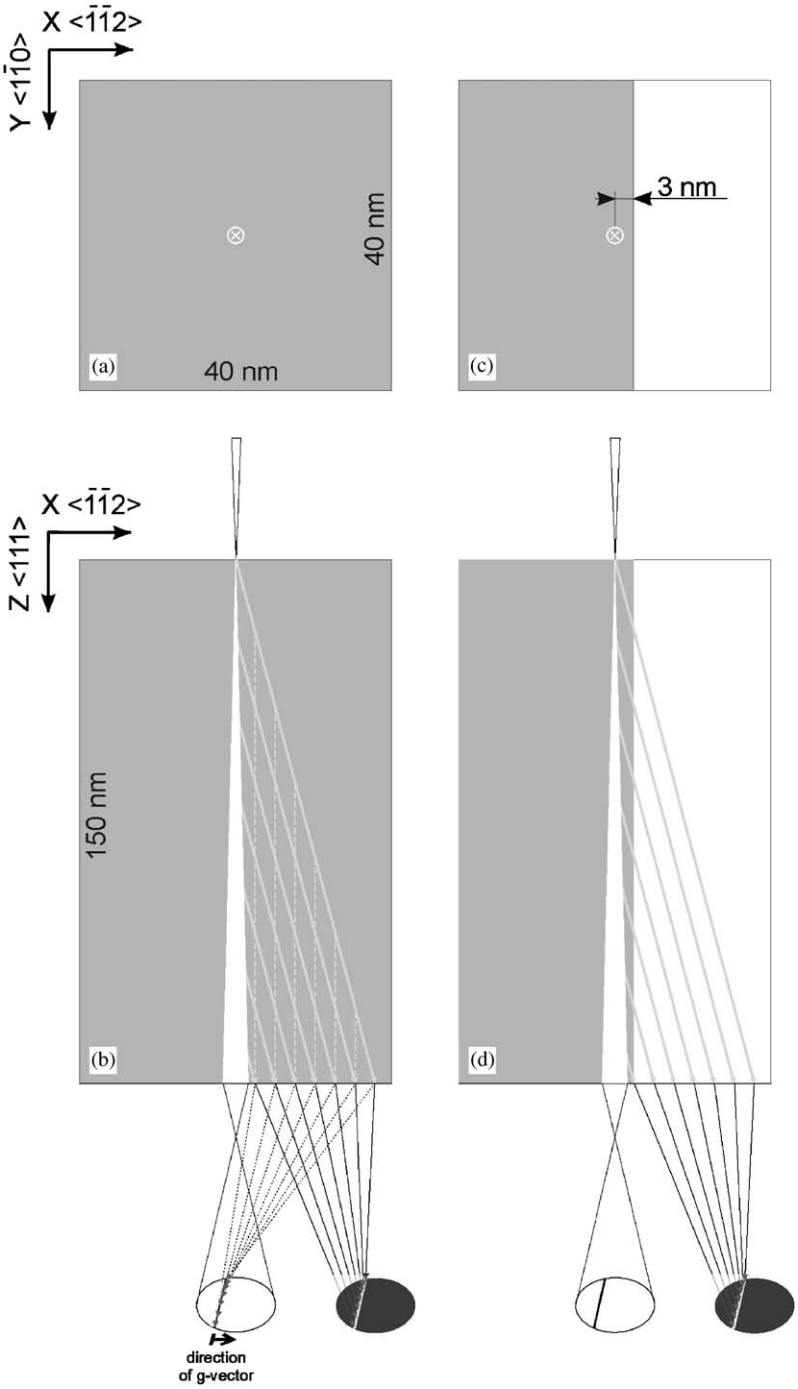

Fig. 6. Scheme of the models used in simulations: (a) perfect Si crystal in [1 1 1] zone viewed in the direction of a beam; dimensions of the supercell are indicated; position of the beam is marked by a cross; (b) side view of the model; scattering of a HOLZ reflection with reciprocal vector **g** is illustrated; probable backscattering of this reflection in the direction of the central beam is indicated by dashed lines; (c) model of the crystal with an edge viewed in the direction of the beam; the edge is as far as 3 nm away from the beam position and (d) side view of the edge model; secondary scattering of HOLZ reflection does not take place because of the lack of scattering media. According to the modern concept for the locality of CBED pattern formation, CBED patterns from both models should be the same, besides the shifts of the *excessive* HOLZ lines due to refraction at the edge.

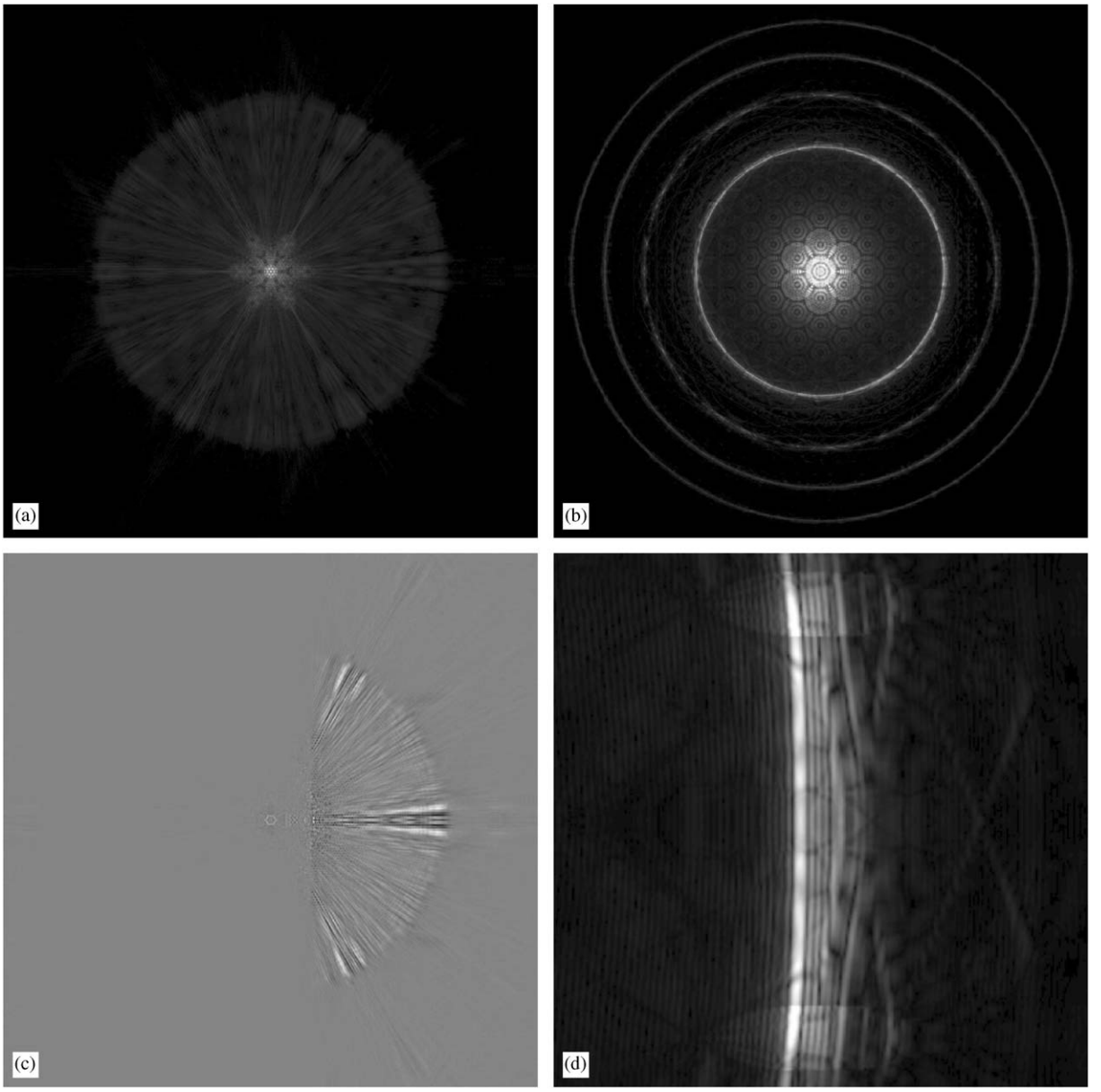

Fig. 7. (a) Exit wave for the case of a probe propagating near the crystal edge, simulation conditions are the same as for Fig. 4, edge of the crystal is 3 nm to the right of the probe position, compare to Fig. 4c, (b) CBED pattern corresponding to (a), compare to Fig. 5a, (c) difference between wave function at (a) and Fig. 4c and (d) $\langle \bar{1}\,1\,5\,5 \rangle$ type excess line, compare to Fig. 5b, the line is no longer a cross-section of dispersion surface, but rather an intersection of Ewald sphere and the first Laue zone.

4. Summary

It has been demonstrated by comparison to Bloch-waves simulation that the inclusion of the new slicing scheme into the multislice algorithm allows CBED pattern simulation including HOLZ lines to a good approximation. The full set of Kikuchi lines can be simulated as well by utilising

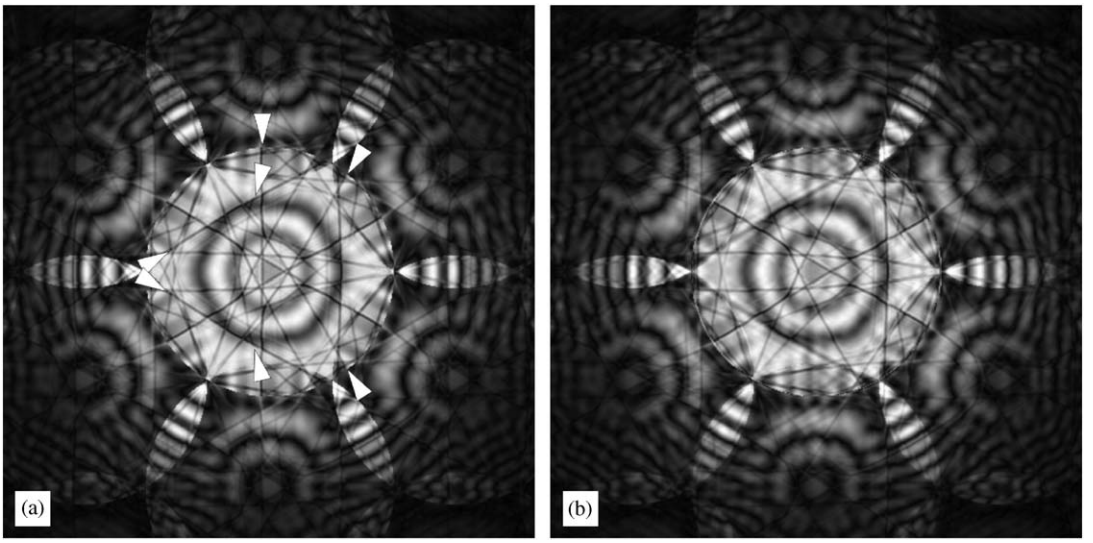

Fig. 8. (a) Central disk of the CBED pattern for the bulk crystal (Fig. 5a), (b) central disk of CBED pattern for the crystal model with the edge (Fig. 7b), note blurring and vanishing of the lines marked by the white arrows in (a).

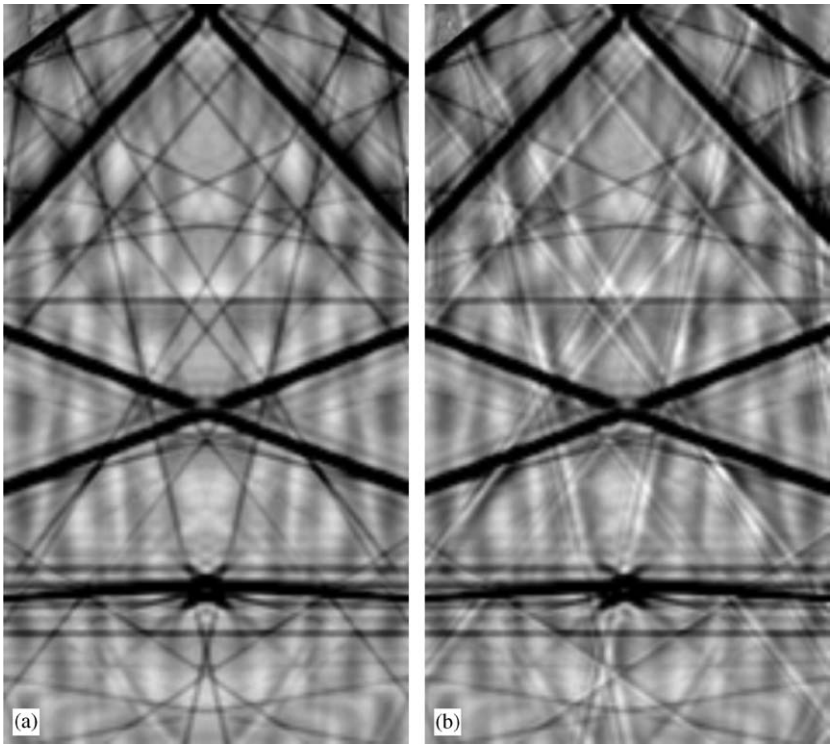

Fig. 9. [3 3 1] Si CBED patterns, accelerating voltage 100 kV, thickness 237 nm, supercell: 47 nm × 47 nm^2, matrix: 4K × 4K: (a) perfect unstrained crystal and (b) crystal with a gradient of strain of 4.3×10^{-4} nm^{-1} in [1 1 0] direction (from left to right at the image); note the symmetry breakage and the line profiles oscillations.

the frozen phonon model. As the multislice approach does not require additional approximations for imperfect structures, CBED patterns for crystals with defects, strain fields, interfaces, etc. can be calculated within the same accuracy as for the perfect crystals.

It was shown that HOLZ lines in the central CBED disk are produced by dynamical scattering of weak HOLZ reflections and thus originate from the whole scattering volume of the HOLZ lines rather than from the scattering volume of the strong beams only. The scattering regions for the different HOLZ lines are different, and, consequently, the central CBED disk represents a combination of structural information from the different azimuths around the illuminating beam. The direct association of line positions and crystal structure may therefore lead to an incorrect interpretation of crystal structure distortions in the presence of a strong strain gradient.

Besides unexpected line shifts, the variation of lattice parameters within the scattering area results also in a deviation of line profiles from the "normal" shape: an additional formfactor (oscillation or splitting) is observed, which reflects the character of the strain distribution. The analysis of the line profiles may provide new possibilities, which then might become an effective tool for the determination of the complete three-dimensional strain field.

Acknowledgements

We acknowledge the valuable and inspiring discussions with Dr. A. Preston, Prof. M. Tanaka and Prof. K. Tsuda. The work was supported by the German Research Foundation DFG KA 1295/2-3.

References

[1] M. Tanaka, Acta Cryst. A 50 (1994) 261.
[2] J. Taftø, J.C.H. Spence, J. Appl. Cryst. 15 (1982) 60.
[3] M. Saunders, A.G. Fox, P.A. Midgley, Acta Cryst. A 55 (1999) 480.
[4] M.-Y. Wu, S.-Y. Li, Zhu. Jing, Z.-H. Du, S.-L. Li, Acta Crystallogr. A 56 (2) (2000) 189.
[5] C. Deininger, J. Mayer, M. Rühle, Optik 99 (4) (1995) 135.
[6] P.A. Midgley, M. Saunders, Contemp. Phys. 37 (6) (1996) 441.
[7] D. Cherns, A.R. Preston, J. Electron Microsc. Tech. 13 (1989) 111.
[8] S. Yamada, M. Tanaka, J. Electron Microsc. 44 (1995) 212.
[9] J.P. Morniroli, D. Cherns, Ultramicroscopy 62 (1996) 53.
[10] J.M. Zuo, M. Kim, R. Holmestad, J. Electron Microsc. 47 (2) (1998) 121.
[11] U. Kaiser, K. Saitoh, K. Tsuda, M. Tanaka, J. Electron Microsc. 48 (3) (1999) 221.
[12] S. Kraemer, J. Mayer, C. Witt, A. Weickenmeier, M. Ruhle, Ultramicroscopy 81 (2000) 245.
[13] A. Armigliato, R. Balboni, G.P. Carnevale, G. Pavia, D. Piccolo, S. Frabboni, A. Benedetti, A.G. Cullis, Appl. Phys. Lett. 82 (13) (2003) 2172.
[14] K. Tsuda, M. Tanaka, Acta Cryst. A 51 (1995) 7.
[15] J.M. Zuo, J.C. Mabon, WebEMAPS software, University of Illinois at Urbana—Champaign; URL: http://emaps.mrl.uiuc.edu/
[16] J.M. Zuo, J.C.H. Spence, Phil. Mag. A 68 (5) (1993) 1055.
[17] F. Banhart, Ultramicroscopy 56 (1994) 233.
[18] R. Pantel, L. Clément, J.L. Rouvière, L.F.Tz. Kwakman, Microsc. Microanal. 9 (Suppl 2) (2003) 866.
[19] Z. Liliental-Weber, T. Kaneyama, M. Terauchi, M. Tanaka, J. Cryst. Growth 132 (1993) 103.
[20] J.C.H. Spence, Acta Cryst. A 34 (1978) 112.
[21] D.A. Muller, B. Edwards, E.J. Kirkland, J. Silcox, Ultramicroscopy 86 (2001) 371.
[22] C. Koch, J.C.H. Spence, C. Zorman, M. Mehregany, J. Chung, J. Phys.: Condens. Matter 12 (2000) 10175.
[23] J.C.H. Spence, C. Koch, Phil. Mag. B 81 (11) (2001) 1701.
[24] E.J. Kirkland, Advanced Computing in Electron Microscopy, Plenum, New York, 1998.
[25] J.M. Cowley, J.C.H. Spence, Ultramicroscopy 3 (1979) 433.
[26] E.J. Kirkland, R.F. Loane, J. Silcox, Ultramicroscopy 23 (1987) 77.
[27] R. Kilaas, M.A. O'Keefe, K.M. Krishnan, Ultramicroscopy 21 (1987) 47.
[28] J.H. Chen, M. Op de Beeck, D. Van Dyck, Microsc. Microanal. Microstruct. 7 (1997) 27.
[29] P.A. Doyle, P.S. Turner, Acta Cryst. A 24 (1967) 390.
[30] R.F. Loane, P. Xu, J. Silcox, Acta Crystallogr. A 47 (1991) 267.
[31] Y. Wakayama, Y. Takahashi, S. Tanaka, Jpn. J. Appl. Phys. 35 (1996) L1662.